

Nuclear matter in the crust of neutron stars

P. Gögelein and H. Mütter

*Institut für Theoretische Physik,
Universität Tübingen,
D-72076 Tübingen, Germany*

The properties of inhomogeneous nuclear matter are investigated considering the self-consistent Skyrme Hartree-Fock approach with inclusion of pairing correlations. For a comparison we also consider a relativistic mean field approach. The inhomogeneous infinite matter is described in terms of cubic Wigner-Seitz cells, which leads to a smooth transition to the limit of homogeneous nuclear matter. The possible existence of various structures in the so-called pasta phase is investigated within this self-consistent approach and a comparison is made to results obtained within the Thomas-Fermi approximation. Results for the proton abundances and the pairing properties are discussed for densities for which clustering phenomena are obtained.

PACS numbers: 21.60.Jz, 21.65.+f, 26.60.+c, 97.60.Jd

I. INTRODUCTION

The crust of neutron stars is a very intriguing object for theoretical nuclear structure physics, as it contains the transition from stable nuclei in the outer crust to a system of homogeneous nuclear matter, consisting of protons, neutrons and leptons in β -equilibrium, in the inner part of this crust. The question of how matter consisting of isolated nuclei melts into uniform matter with increasing density has evoked a large number of studies[1, 2, 3, 4]. Already at moderate densities the Fermi energy of the electron is so high that the β -stability enhances the neutron fraction of the baryons so much that a part of these neutrons drip out of the nuclei. This leads to a structure, in which quasi-nuclei, clusters of protons and neutrons, are embedded in a sea of neutrons. In order to minimise the Coulomb repulsion between the protons, the quasi-nuclei form a lattice.

Therefore one typically describes these structures in form of the Wigner-Seitz (WS) cell approximation. One assumes a geometrical shape for the quasi-nuclei and determines the nuclear contribution to the energy of such a WS cell from a phenomenological energy-density functional. Such Thomas-Fermi calculations yield a variety of structures: Spherical quasi-nuclei, which are favoured at small densities, merge with increasing density to strings, which then may cluster to parallel plates and so on. These geometrical structures have been the origin for the popular name of this phase: Pasta phase.

Such Thomas-Fermi calculations, however, are very sensitive to the surface tension under consideration. Furthermore they do not account for characteristic features of the structure of finite nuclei, like the shell-effects. Shell effects favour the formation of closed shell systems and may have a significant effect on the formation of inhomogeneous nuclear structures in the crust of neutron stars. These shell effects are incorporated in self-consistent Hartree-Fock or mean field calculations, which can treat finite nuclei, infinite matter and inhomogeneous structures in between within a consistent frame based on an effective nucleon-nucleon interaction. Such calculations employing the density-dependent Skyrme forces[5, 6] have been

done more than 25 years ago by Bonche and Vautherin[7] and by a few other groups.

These studies show indeed that shell effects have a significant influence on details like the proton fraction of the baryonic matter in the inhomogeneous phase[8]. They also provide the basis for a microscopic investigation of properties beyond the equation of state. This includes the study of pairing phenomena, excitation modes and response functions as well as the effects of finite temperature.

Self-consistent Hartree-Fock calculations for such inhomogeneous nuclear structures have typically been performed assuming a WS cell of spherical shape. This assumption of quasi-nuclei with spherical symmetry reduces the numerical work-load considerably. However, it does not allow the exploration of quasi-nuclear clusters in form of strings or plates as predicted from Thomas-Fermi calculations. Furthermore the limit of homogeneous matter can not be described in a satisfactory manner in such a spherical WS cell. Employing the representation of plane wave single-particle states in terms of spherical Bessel functions leads to a density profile, which, depending on the boundary condition chosen, exhibits either a minimum or a maximum at the boundary of the cell. Bonche and Vautherin[7] therefore suggested to use a mixed basis, for which, depending on the angular momentum, different boundary conditions were considered. However, even this optimised choice leads to density profiles with fluctuations[8].

Therefore the investigations presented here consider cubic WS cells, which allows for the description of non-spherical quasi-nuclear structures and contains the limit of homogeneous matter in a natural way. Self-consistent Hartree-Fock calculations are performed for β -stable matter at densities for which the quasi-nuclear structures discussed above are expected. For the nuclear Hamiltonian we consider various Skyrme forces but also perform calculations within the effective relativistic mean-field approximation. Special attention will be paid to the comparison between results obtained in the Hartree-Fock approach and corresponding Thomas-Fermi calculations.

After this introduction we will briefly review the Hartree-Fock approximation using Skyrme interactions and the technique used to solve the equations resulting from this approach employing the imaginary time step method in section 2. We then turn to the relativistic mean field approach and the adaption of the imaginary time step method to be used within this relativistic framework. After a short description on the inclusion of pairing correlations in section 4, we present results in section 5. The main conclusions are summarised in the final section 6.

II. SKYRME-HARTREE-FOCK CALCULATIONS

A. Energy Functional

The Skyrme-Hartree-Fock approach has frequently been described in the literature[5, 6, 7, 9]. Therefore we will restrict the presentation here to a few basic equations, which will define the nomenclature. The Skyrme model is defined in terms of an energy density $\mathcal{H}(\mathbf{r})$, which can be split into various contributions[6, 10]

$$\mathcal{H} = \mathcal{H}_K + \mathcal{H}_0 + \mathcal{H}_3 + \mathcal{H}_{\text{eff}} + \mathcal{H}_{\text{fin}} + \mathcal{H}_{\text{so}} + \mathcal{H}_{\text{Coul}}, \quad (1)$$

where \mathcal{H}_K is the kinetic energy term, \mathcal{H}_0 a zero range term, \mathcal{H}_3 a density dependent term, \mathcal{H}_{eff} an effective mass term, \mathcal{H}_{fin} a finite range term and \mathcal{H}_{so} a spin-orbit term. These terms

are given by

$$\begin{aligned}
\mathcal{H}_K &= \frac{\hbar^2}{2m}\tau, \\
\mathcal{H}_0 &= \frac{1}{4}t_0[(2+x_0)\rho^2 - (2x_0+1)(\rho_p^2 + \rho_n^2)], \\
\mathcal{H}_3 &= \frac{1}{24}t_3\rho^\alpha[(2+x_3)\rho^2 - (2x_3+1)(\rho_p^2 + \rho_n^2)], \\
\mathcal{H}_{\text{eff}} &= \frac{1}{8}[t_1(2+x_1) + t_2(2+x_2)]\tau\rho \\
&\quad + \frac{1}{8}[t_2(2x_2+1) - t_1(2x_1+1)][\tau_p\rho_p + \tau_n\rho_n], \\
\mathcal{H}_{\text{fin}} &= -\frac{1}{32}[3t_1(2+x_1) - t_2(2+x_2)]\rho\Delta\rho \\
&\quad + \frac{1}{32}[3t_1(2x_1+1) + t_2(2x_2+1)][\rho_p\Delta\rho_p + \rho_n\Delta\rho_n], \\
\mathcal{H}_{\text{so}} &= -\frac{1}{2}W_0[\rho\nabla\mathbf{J} + \rho_p\nabla\mathbf{J}_p + \rho_n\nabla\mathbf{J}_n].
\end{aligned} \tag{2}$$

The coefficients t_i , x_i , W_0 , and α are the parameters of a generalised Skyrme force[11]. The energy density of eq.(1) contains furthermore the contribution of the Coulomb force, $\mathcal{H}_{\text{Coul}}$, which is calculated from the charge density ρ_C as

$$\mathcal{H}_{\text{Coul}} = \frac{e^2}{2}\rho_C(\mathbf{r}) \int d^3r' \frac{\rho_C(\mathbf{r}')}{|\mathbf{r} - \mathbf{r}'|} - \frac{3e^2}{4} \left(\frac{3}{\pi}\right)^{1/3} \rho_C^{4/3}. \tag{3}$$

Here the exchange part of the Coulomb term is calculated within the Slater approximation. Following [11] the center-of-mass recoil energy has been approximated as $-\sum \mathbf{p}_i^2/2Am$.

The densities ρ , τ , and \mathbf{J} are defined in terms of the corresponding densities for protons and neutrons $\rho = \rho_p + \rho_n$, $\tau_p + \tau_n$ and $\mathbf{J} = \mathbf{J}_p + \mathbf{J}_n$. If we identify the isospin label ($q = n, p$), the corresponding matter densities are given by

$$\rho_q(\mathbf{r}) = \sum_{k,s} \eta_k^q |\varphi_k^q(\mathbf{r}, s)|^2, \tag{4}$$

where $\varphi_k^q(\mathbf{r}, s)$ is the single-particle wave function with orbital, spin and isospin quantum numbers k , s and q . The occupation factors η_k^q are determined by the Fermi energy and the desired scheme of occupation (see discussion below). The kinetic energy and spin-orbit densities are defined by

$$\tau_q(\mathbf{r}) = \sum_{k,s} \eta_k^q |\nabla\varphi_k^q(\mathbf{r}, s)|^2, \tag{5}$$

$$\mathbf{J}_q(\mathbf{r}) = -i \sum_{k,s,s'} \eta_k^q (\varphi_k^q)^*(\mathbf{r}, s') \nabla\varphi_k^q(\mathbf{r}, s) \times \langle s' | \boldsymbol{\sigma} | s \rangle. \tag{6}$$

The gradient of the spin-orbit density $\nabla\mathbf{J} = \nabla\mathbf{J}_p + \nabla\mathbf{J}_n$ can be directly evaluated without first calculating \mathbf{J} :

$$\nabla\mathbf{J}_q(\mathbf{r}) = -i \sum_{k,s,s'} \eta_k^q \nabla(\varphi_k^q)^*(\mathbf{r}, s') \times \nabla\varphi_k^q(\mathbf{r}, s) \cdot \langle s' | \boldsymbol{\sigma} | s \rangle. \tag{7}$$

We left out the spin-gradient term [10], which is cumbersome to evaluate in three-dimensional calculations numerically and not very important.

The single-particle wave functions are determined as solutions of the Hartree-Fock equations

$$\left\{ -\nabla \frac{\hbar^2}{2m_q^*(\mathbf{r})} \nabla + U_q(\mathbf{r}) - i \mathbf{W}_q(\mathbf{r}) \cdot (\nabla \times \boldsymbol{\sigma}) \right\} \varphi_k^q(\mathbf{r}) = \varepsilon_k^q \varphi_k^q(\mathbf{r}, s), \quad (8)$$

with an effective mass term $m^*(\mathbf{r})$, which depends on the \mathcal{H}_{eff} part of the energy density functional

$$\begin{aligned} \frac{\hbar^2}{2m_q^*(\mathbf{r})} &= \frac{\hbar^2}{2m} + \frac{1}{8}[t_1(2+x_1) + t_2(2+x_2)] \rho(\mathbf{r}) \\ &\quad + \frac{1}{8}[t_2(1+2x_2) - t_1(1+2x_1)] \rho_q(\mathbf{r}), \end{aligned} \quad (9)$$

a nuclear central Potential

$$\begin{aligned} U_q(\mathbf{r}) &= \frac{1}{2}t_0[(2+x_0)\rho - (1+2x_0)\rho_q] \\ &\quad + \frac{1}{24}t_3(2+x_3)(2+\alpha)\rho^{\alpha+1} \\ &\quad - \frac{1}{24}t_3(2x_3+1)[2\rho^\alpha\rho_q + \alpha\rho^{\alpha-1}(\rho_p^2 + \rho_n^2)] \\ &\quad + \frac{1}{8}[t_1(2+x_1) + t_2(2+x_2)] \tau \\ &\quad + \frac{1}{8}[t_2(2x_2+1) - t_1(2x_1+1)] \tau_q \\ &\quad + \frac{1}{16}[t_2(2+x_2) - 3t_1(2+x_1)] \Delta\rho \\ &\quad + \frac{1}{16}[3t_1(2x_1+1) + t_2(2x_2+1)] \Delta\rho_q \\ &\quad - \frac{1}{2}W_0[\nabla \mathbf{J} + \nabla \mathbf{J}_q] \\ &\quad + \delta_{q,p}V_{\text{Coul}} \end{aligned} \quad (10)$$

with the Coulomb field

$$V_{\text{Coul}}(\mathbf{r}) = e^2 \int d^3r' \frac{\rho_C(\mathbf{r}')}{|\mathbf{r} - \mathbf{r}'|} - e^2 \left(\frac{3}{\pi} \right)^{1/3} \rho_C^{1/3} \quad (11)$$

and a spin-orbit field:

$$\mathbf{W}_q(\mathbf{r}) = \frac{1}{2} W_0 (\nabla \rho + \nabla \rho_q) \quad (12)$$

B. Imaginary Time Step

Various different methods have been developed to solve the Hartree-Fock equations. Frequently the single-particle wave functions are expanded in a basis like e.g. the eigenfunctions of an appropriate harmonic oscillator. This is appropriate for describing the wave functions for single-particle states, which are deeply bound. It is not so appropriate for the description of weakly bound or unbound single-particle states, since the asymptotic behaviour of the harmonic oscillator basis states is not appropriate for these states.

This can be cured by employing the eigenstates of a spherical box with an appropriate radius R [8], which can also be considered as a Wigner Seitz cell for describing periodic systems. Such a spherical box, however, is not appropriate for the description of deformed nuclei and nuclear structures as they are expected for the pasta phase in the crust of neutron stars. This, as well as the problems with the boundary conditions in a spherical WS cell discussed already in the introduction calls for a cartesian WS cell.

The single-particle wave functions in such a cartesian WS cell can be represented by its values on a discretized mesh in this cell. The spacings between the mesh points, Δx , Δy and Δz correspond to truncations in momentum space. Smaller values for these spacings account for larger momentum components in the wave functions. The obvious disadvantage of such calculations is the huge amount of mesh points which has to be taken into account. Therefore one needs a fast iterative procedure for the solution of the self-consistent Hartree-Fock equations, which evaluates only the desired states.

Davies et al. presented in [12] an efficient method for this problem, the *imaginary time step method*, which we want to outline briefly. The origin for the name of this method is the analogy to the time-dependent Hartree-Fock (TDHF) method which solves the equations

$$i\hbar \frac{\partial \varphi_k}{\partial t} = H(t) \varphi_k(t), \quad k = 1, \dots, A \quad (13)$$

for an orthonormal set of A wave functions $\{\varphi_k\}$, and a Hamiltonian H which depends on the time t . This is the case when we identify $H(t)$ e.g. with the Hartree-Fock (HF) Hamiltonian represented in eq.(8), which depends on t as it depends on the resulting wave-function $\varphi_k(t)$ in a self-consistent way. These equations are discretized in time introducing a time step Δt , with $t_n = n \Delta t$. Then the time evolution of the set of wave functions $\{\varphi_k\}$ may be approximated by the iterative procedure

$$|\varphi_k^{(n+1)}\rangle = \exp\left(-\frac{i}{\hbar} \Delta t H^{(n+\frac{1}{2})}\right) |\varphi_k^{(n)}\rangle, \quad k = 1, \dots, A \quad (14)$$

in which $\varphi_k^{(n)}$ represents the wave-function φ_k at the time t_n and $H^{(n+\frac{1}{2})}$ denotes the numerical approximation to the Hamiltonian $H(t)$ at the time $(n+\frac{1}{2})\Delta t$. The idea of Davies et al. was to replace the time step Δt by the imaginary quantity $-i\Delta t$. Introducing the positive parameter $\lambda = \Delta t/\hbar$ the procedure for the imaginary time step gets

$$|\tilde{\varphi}_k^{(n+1)}\rangle = \exp\left(-\lambda H^{(n+\frac{1}{2})}\right) |\varphi_k^{(n)}\rangle, \quad k = 1, \dots, A \quad (15)$$

where $\{\tilde{\varphi}_k^{(n+1)}\}$ is not any more an orthonormal set of wave functions since the imaginary time operator $\exp(-\lambda H^{(n+\frac{1}{2})})$ is not unitary. Applying the Gram-Schmidt orthonormalization method \mathcal{O} we get the orthonormal set $\{\varphi_k^{(n+1)}\}$ by

$$|\varphi_k^{(n+1)}\rangle = \mathcal{O}|\tilde{\varphi}_k^{(n+1)}\rangle \quad k = 1, \dots, A. \quad (16)$$

This procedure converges leading to those eigenfunctions of the Hamiltonian H , which correspond to the lowest A eigenvalues of the Hamiltonian H .

In practical applications the Hamiltonian $H^{(n+\frac{1}{2})}$ is replaced by the Hamiltonian $H^{(n)}$ of the n -th step, which makes the calculation fast keeping the algorithm stable. After this replacement, we get the following operation on the wave functions

$$\varphi_k^{(n+1)} = \mathcal{O}\left(\exp(-\lambda H^{(n)}) \varphi_k^{(n)}\right) \quad k = 1, \dots, A, \quad (17)$$

For numerical application one has to truncate the exponential series to a certain order. In earlier HF calculations the gradient method was used with the operation $\mathcal{O}(1 - \lambda H)$ on the wave functions ([9]). If one truncates the exponential series in the imaginary time step going

beyond the first order one obtains an improvement of the gradient method. Davies et al. recommended a truncation to 4th or 5th order for a HF calculation of ^{40}Ca together with a time step $\Delta t = 4.0 \times 10^{-24} \text{ s}$ and a mesh size of 1.0 fm.

In our calculations we used the same mesh size as Davies et al. but the convergence got worse since we consider in our studies a larger number of nucleons, which implies a larger number of wave functions A have to be evolved. Hence we truncated the exponential operator at 9th order and the time step Δt was set to $2.0 \times 10^{-24} \text{ s}$. For the check of convergence the mean square deviation of the single particle energies for N Nucleons and η_k the occupation probability is calculated by

$$\Delta H^{(n)} = \left(\frac{1}{A} \sum_{k=1}^A \eta_k \left(\langle \varphi_k^{(n)} | H^{(n)} | \varphi_k^{(n)} \rangle - \langle \varphi_k^{(n)} | H^{(n)} | \varphi_k^{(n)} \rangle^2 \right) \right)^{\frac{1}{2}} \quad (18)$$

which provides a better criterion as calculating energy differences.

The HF equations have been solved by discretization in coordinate space within a cubic Wigner–Seitz cell similar to [11] with periodic boundary conditions. The box sizes typically considered vary from $2 \times 10 \text{ fm}$ to $2 \times 16 \text{ fm}$. This technique is able to allow for general deformations of the quasi-nuclear structures. The densities we are considering requires to account for around 1500 nucleons, which implies that up to $A = 2600$ wave functions had to be evolved to account for pairing correlations with occupation probabilities η_k different from zero.

To decrease the numerical effort we assume two symmetries like in [11]:

- parity

$$\hat{P} \varphi_k(\mathbf{r}, s) = \varphi_k(-\mathbf{r}, s) = p_k \varphi_k(\mathbf{r}, s), \quad p_k = \pm 1; \quad (19)$$

- z-signature

$$\begin{aligned} \exp\{i\pi(\hat{J}_z - \tfrac{1}{2})\} \varphi_k(x, y, z, s) &= \sigma \varphi_k(-x, -y, z, s) \\ &= \eta_k \varphi_k(x, y, z, s), \quad \eta_k = \pm 1. \end{aligned} \quad (20)$$

These symmetries still allow triaxial deformations and reduce the calculation to the positive coordinates in each direction. As additional symmetry time-reversal-invariance is assumed for the time-reversed pairs φ_k , and $\varphi_{\bar{k}}$:

$$\varphi_{\bar{k}}(\mathbf{r}, s) = (\hat{T} \varphi_k)(\mathbf{r}, s) = \sigma \varphi_k^*(\mathbf{r}, -s). \quad (21)$$

Summarising this symmetries it is sufficient to solve the HF equations for one wave function of the time-reversed pairs. We choose the positive z-signature orbital for which we get the symmetries summarised in table I. The wave functions $\varphi_k(\mathbf{r}, s)$ are realized as complex Pauli spinors. The reflections at the $x = 0$ and $y = 0$ planes are realized by the parity operator of the real part together with complex conjugation.

The iteration is performed with accurate numerical methods. For the differential operators 11-point formulas are used, which have been derived by eliminating errors for functions f with $f(x) = x^n$ up to a certain $n_0 \in \mathbb{N}$. The ansatz for the numerical approximation of the derivatives on an equidistant mesh with the points x_i and $f_i = f(x_i)$ is for the first derivative

$$\frac{\partial}{\partial x} f(x_i) \approx \left(\frac{\partial}{\partial x} \right)_{\text{num}} f(x_i) = \sum_{j=1}^N a_j \frac{1}{2j\Delta x} (f_{i+j} - f_{i-j}), \quad (22)$$

	x=0	y=0	z=0
Re $\varphi_k(\mathbf{r}, +\frac{1}{2})$	+	+	p_k
Im $\varphi_k(\mathbf{r}, +\frac{1}{2})$	-	-	p_k
Re $\varphi_k(\mathbf{r}, -\frac{1}{2})$	-	+	$-p_k$
Im $\varphi_k(\mathbf{r}, -\frac{1}{2})$	+	-	$-p_k$

TABLE I: Parity properties of the Pauli spinors with respect to the coordinate planes

with $N = 5$ for 11-point formula and a_j the coefficients of the formula. Requiring that the approximation gets equal up to a certain $n_0 \in \mathbb{N}$ we obtain a linear equation. Inserting the result in the ansatz we finally obtain

$$\begin{aligned} & \left(\frac{\partial}{\partial x} \right)_{\text{num}} f(x_i) \\ &= \frac{1}{\Delta x} \left(\frac{1}{19860} (11f_{i+5} - 4500f_{i+2} + 16350f_{i+1} \right. \\ & \quad \left. - 16350f_{i-1} + 4500f_{i-2} - 11f_{i-5}) \right. \\ & \quad \left. + \frac{1}{55608} (-445f_{i+4} + 2950f_{i+3} - 2950f_{i-3} + 445f_{i-4}) \right). \end{aligned} \quad (23)$$

For the second derivative used in the laplacian the ansatz is

$$\frac{\partial}{\partial x} f(x_i) \approx \left(\frac{\partial}{\partial x} \right)_{\text{num}} f(x_i) = \sum_{j=1}^N a_j \frac{1}{(j \Delta x)^2} (f_{i+j} - 2f_i + f_{i-j}). \quad (24)$$

and finally the formula gets

$$\begin{aligned} & \left(\frac{\partial^2}{\partial x^2} \right)_{\text{num}} f(x_i) \\ &= \frac{1}{(\Delta x)^2} \left(\frac{1}{49650} (11f_{i+5} - 11250f_{i+2} + 81750f_{i+1} \right. \\ & \quad \left. + 81750f_{i-1} - 11250f_{i-2} + 11f_{i-5}) - \frac{1729639}{595800} f_i \right. \\ & \quad \left. + \frac{1}{333648} (-1335f_{i+4} + 11800f_{i+3} + 118002950f_{i-3} - 1335f_{i-4}) \right). \end{aligned} \quad (25)$$

In the case of the Wigner-Seitz cell calculations charge neutrality is assumed and electrons are taken into account as relativistic Fermi gas which contribute to the charge density $\rho_C(\mathbf{r}) = \rho_p(\mathbf{r}) - \rho_e$. For the calculation of finite nuclei the electrons are not taken into account ($\rho_e = 0$).

There are different methods to solve the Poisson equation

$$-\Delta V_C(\mathbf{r}) = 4\pi\rho_c(\mathbf{r}). \quad (26)$$

It turned out that the numerically most accurate and stable method is the integration applying the Green's function for this problem

$$V_C(\mathbf{r}) = \int_V d\mathbf{r}'^3 \rho_C(\mathbf{r}') \frac{1}{|\mathbf{r} - \mathbf{r}'|}. \quad (27)$$

Unfortunately, this integral has lots of singularities, but it can be rewritten. First, the Green's function is written as ([13]):

$$\frac{1}{|\mathbf{r} - \mathbf{r}'|} = \frac{1}{2} \Delta_{\mathbf{r}'} |\mathbf{r} - \mathbf{r}'|. \quad (28)$$

Then the integral is transformed by Green's theorem for scalar functions f and g defined on a Volume V with closed surface $A = \partial V$ ([14]):

$$\int_V dV (f \Delta g) - \int_V dV (g \Delta f) = \oint_{A=\partial V} d\mathbf{A} \cdot (f \nabla g - g \nabla f). \quad (29)$$

Identifying and $f = \rho_C(\mathbf{r}')$ and $g = \frac{1}{2}|\mathbf{r} - \mathbf{r}'|$ the final result gets

$$\begin{aligned} V_C(\mathbf{r}) = & \frac{1}{2} \int_V dr'^3 \Delta \rho_C(\mathbf{r}') |\mathbf{r} - \mathbf{r}'| \\ & + \frac{1}{2} \oint_{A=\partial V} d\mathbf{A} \cdot (\rho_C(\mathbf{r}') \nabla_{\mathbf{r}'} |\mathbf{r} - \mathbf{r}'| - |\mathbf{r} - \mathbf{r}'| \nabla_{\mathbf{r}'} \rho_C(\mathbf{r}')), \end{aligned} \quad (30)$$

which has no singularities. Altogether the result of this transformation behaves very well in numerical calculations and the numerical result is practically the same as the exact one. For finite nuclei it is possible to drop the boundary integrals as has already been discussed by Vautherin [13].

We tested the computer program for the parameter set Skyrme III by comparing results for finite nuclei with those of [11]. Additional tests have been performed using the parameter set SLy4 [10].

III. RELATIVISTIC MEAN FIELD CALCULATIONS

In order to test the sensitivity of the results on the model under consideration we also investigated the quasi-nuclear structures in the crust of neutron stars employing the relativistic mean field approach in a cubic box.

A. From the Lagrangian to the Dirac Equation

The relativistic mean field approach is based on a Lagrangian is similar to that in [15] and consists of three parts: Lagrangian for the free baryons \mathcal{L}_B , the free mesons \mathcal{L}_M and the interaction Lagrangian \mathcal{L}_{int} :

$$\mathcal{L} = \mathcal{L}_B + \mathcal{L}_M + \mathcal{L}_{\text{int}}, \quad (31)$$

which take the form

$$\begin{aligned} \mathcal{L}_B = & \bar{\Psi} (i \gamma_\mu \partial^\mu - m) \Psi, \\ \mathcal{L}_M = & \frac{1}{2} \left(\partial_\mu \Phi_\sigma \partial^\mu \Phi_\sigma - m_\sigma^2 \Phi_\sigma^2 \right) \\ & - \frac{1}{2} \sum_{\kappa=\omega, \rho, \gamma} \left(\frac{1}{2} F_{\mu\nu}^{(\kappa)} - m_\kappa^2 A_\mu^{(\kappa)} A^{(\kappa)\mu} \right), \\ \mathcal{L}_{\text{int}} = & - \bar{\Psi} g_\sigma \Phi_\sigma \Psi - \bar{\Psi} g_\omega \gamma_\mu A^{(\omega)\mu} \Psi \\ & - \bar{\Psi} \frac{1}{2} g_\rho \gamma_\mu \boldsymbol{\tau} \mathbf{A}^{(\rho)\mu} \Psi - \bar{\Psi} e \gamma_\mu \frac{1}{2} (1 + \tau_3) A^{(\gamma)\mu} \Psi, \end{aligned} \quad (32)$$

with the field strength tensor $F_{\mu\nu}^{(\kappa)} = \partial_\mu A_\nu^{(\kappa)} - \partial_\nu A_\mu^{(\kappa)}$, the meson fields Φ_σ , $A^{(\omega)}$, $\mathbf{A}^{(\rho)}$ and the electromagnetic field $A^{(\gamma)}$. The bold symbols are isovectors, the γ^μ are the Dirac γ matrices and Ψ is a nucleon field which consists of Dirac 4-spinors with isospin space. The masses are the baryon mass $m = 938.9 \text{ MeV}$ and the meson masses $m_\sigma = 520 \text{ MeV}$, $m_\omega = 783 \text{ MeV}$ and $m_\rho = 770 \text{ MeV}$ according to a parameter set for the linear model from Horowitz and Serot [16] cited as L-HS in [15]. The coupling constants of this parameter set are $g_\sigma = 10.4814$, $g_\omega = 13.8144$ and $g_\rho = 8.08488$. The charge of the electron $e = \sqrt{\alpha \hbar c / 4\pi}$ where α is the fine structure constant and $\hbar c = 197.32 \text{ MeV fm}$.

Applying the equations of motion and taking the static limit we obtain in the Hartree approximation the static Dirac equation ([17])

$$\varepsilon_\alpha \psi_\alpha = (\boldsymbol{\alpha} \mathbf{p} + V + \beta(m - S)) \psi_\alpha. \quad (33)$$

where α and β are matrices like in [18], ε_α the single-particle energy of the state ψ_α , \mathbf{p} the momentum operator and S and V the scalar and vector fields

$$\begin{aligned} S &= -g_\sigma \Phi_\sigma \\ V &= g_\omega A_0^{(\omega)} + \frac{1}{2} g_\rho \tau_3 A_0^{(\rho)} + e \frac{1}{2} (1 - \tau_3) A_0^{(\gamma)}. \end{aligned} \quad (34)$$

For the mesons fields we get Klein-Gordon-equations. After neglecting retardation effects and taking the Hartree-approximation the meson field equations read

$$\begin{aligned} (-\Delta + m_\sigma^2) \Phi_\sigma &= -g_\sigma \rho^s \\ (-\Delta + m_\omega^2) A_0^{(\omega)} &= g_\omega \rho \\ (-\Delta + m_\rho^2) A_0^{(\rho)} &= \frac{1}{2} g_\rho \rho_3 \\ -\Delta A_0^{(\gamma)} &= e \rho_C \end{aligned} \quad (35)$$

with the scalar density ρ^s , the baryon density ρ , the The densities are calculated taking into account only the occupied positive energy states in the Fermi-sea and neglecting the negative energy states in the Dirac-sea ("No-sea" approximation)

$$\begin{aligned} \rho^s &= \sum_{\alpha=1}^N \eta_\alpha \bar{\psi}_\alpha \psi_\alpha \\ \rho &= \sum_{\alpha=1}^N \eta_\alpha \bar{\psi}_\alpha \gamma_0 \psi_\alpha \\ \rho_3 &= \sum_{\alpha=1}^N \eta_\alpha \bar{\psi}_\alpha \tau_3 \gamma_0 \psi_\alpha \\ \rho_C &= \sum_{\alpha=1}^N \eta_\alpha \bar{\psi}_\alpha \frac{1}{2} (1 - \tau_3) \gamma_0 \psi_\alpha \quad (-\rho_e), \end{aligned}$$

where η_α are the occupation numbers determined by the BCS-formalism. The electron density ρ_e has been considered for the Wigner-Seitz cell calculations but not for studies of finite nuclei.

B. Solving the Triaxial Dirac Equation

The solution of the Dirac equation for nucleons in a cubic box differs of course in some aspects from that in the spherical one. Therefore we briefly outline the numerical solution in the following.

We decompose ψ_α in an upper and lower component Pauli spinor:

$$\psi_\alpha = \begin{pmatrix} \varphi_\alpha \\ \chi_\alpha \end{pmatrix} \quad (36)$$

Hence after applying the transformation $\varepsilon_\alpha \rightarrow \varepsilon_\alpha - m$ to energy levels without rest-mass the Dirac equation becomes

$$\begin{aligned} \varepsilon_\alpha \varphi_\alpha &= \boldsymbol{\sigma} \mathbf{p} \chi_\alpha + U_\varphi \varphi_\alpha \\ \varepsilon_\alpha \chi_\alpha &= \boldsymbol{\sigma} \mathbf{p} \varphi_\alpha + U_\chi \chi_\alpha \end{aligned} \quad (37)$$

with the potentials

$$\begin{aligned} U_\varphi &= -S + V \\ U_\chi &= -2m + S + V. \end{aligned} \quad (38)$$

Now we obtain an "effective Schroedinger equation" by inserting the lower component into the equation for the upper one. This method is according to Reinhard [15] the most efficient way to solve the Dirac equation. First we modify the lower component

$$(\varepsilon_\alpha - U_\chi) \chi_\alpha = \boldsymbol{\sigma} \mathbf{p} \varphi_\alpha \quad (39)$$

then we introduce an "effective mass term" which depends on the wave function

$$\mathcal{B}_\alpha = \frac{1}{\varepsilon_\alpha - U_\chi} \quad (40)$$

and finally get the "effective Schroedinger equation"

$$\varepsilon_\alpha \varphi_\alpha = \boldsymbol{\sigma} \mathbf{p} \mathcal{B}_\alpha \boldsymbol{\sigma} \mathbf{p} \varphi_\alpha + U_\varphi \varphi_\alpha. \quad (41)$$

So far the procedure corresponds to the method employed in calculations assuming spherical symmetry[19]. Using the discretization in a cartesian box, however, requires a different treatment of angular momentum and spin-orbit terms. With the help of the following formula for vector fields \mathbf{A} and \mathbf{B} commuting with $\boldsymbol{\sigma}$

$$\boldsymbol{\sigma} \mathbf{A} \boldsymbol{\sigma} \mathbf{B} = \mathbf{A} \mathbf{B} + i \boldsymbol{\sigma} (\mathbf{A} \times \mathbf{B}) \quad (42)$$

we obtain from the relativistic kinetic energy term

$$\boldsymbol{\sigma} \mathbf{p} \mathcal{B}_\alpha \boldsymbol{\sigma} \mathbf{p} \varphi_\alpha = -\nabla \mathcal{B}_\alpha \nabla \varphi_\alpha - i (\nabla \mathcal{B}_\alpha) \cdot (\nabla \times \boldsymbol{\sigma}) \varphi_\alpha \quad (43)$$

which is like the non-relativistic kinetic energy term plus the spin-orbit term for the upper component. From a further modification we obtain an expression called "effective Hamiltonian" ready for implementation

$$H_{\varphi,\alpha} \varphi_\alpha = -\mathcal{B}_\alpha \Delta \varphi_\alpha - (\nabla \mathcal{B}_\alpha) \cdot (\nabla \varphi_\alpha) - i (\nabla \mathcal{B}_\alpha) \cdot (\nabla \times \boldsymbol{\sigma}) \varphi_\alpha + U_\varphi \varphi_\alpha. \quad (44)$$

In order to calculate the eigenvalue ε_α we can't use the "effective Hamiltonian" like a normal Hamiltonian because we have to take into account the effects of the lower component. This we do in the following manner:

$$\chi_\alpha = \mathcal{B}_\alpha \boldsymbol{\sigma} \mathbf{p} \varphi_\alpha \quad (45)$$

and hence the next approximation of the eigenvalue $\varepsilon_\alpha^{(n+1)}$ in the iteration scheme gets

$$\varepsilon_\alpha^{(n+1)} = \int d^3r \left(\varphi_\alpha^* H_{\varphi,\alpha} \varphi_\alpha + \varepsilon_\alpha^{(n)} \chi_\alpha^* \chi_\alpha \right) \quad (46)$$

This means that in the lower component the whole new information is contained in the new Pauli spinor. The total binding energy is calculated like in [20] using cartesian coordinates

$$\begin{aligned} E = \sum_\alpha \eta_\alpha \varepsilon_\alpha - \frac{1}{2} \int d^3r \left(-g_\sigma \Phi_\sigma(\mathbf{r}) \rho^s(\mathbf{r}) \right. \\ \left. + g_\omega A_0^{(\omega)} \rho(\mathbf{r}) + \frac{1}{2} g_\rho A_0^{(\rho)} \rho_3(\mathbf{r}) + e A_0^{(\gamma)} \rho_C(\mathbf{r}) \right) \\ + E_{\text{cm}} + E_{\text{pair}} \end{aligned} \quad (47)$$

with a center of mass correction in the case of finite nuclei

$$E_{\text{cm}} = -\frac{3}{4} \hbar \omega \quad \text{with} \quad \hbar \omega = 41 A^{-1/3} \text{ MeV} \quad (48)$$

in compliance with [21] and a pairing energy E_{pair} described in the next section.

For the variation of the wave functions in the cubic box we employ once more the imaginary time step in the following manner: First we operate on the upper component with the imaginary time step and the "effective Hamiltonian":

$$\varphi_\alpha^{(n+1)} = \exp(-\lambda H_{\varphi,\alpha}) \varphi_\alpha^{(n)} \quad (49)$$

then the lower component is calculated:

$$\chi_\alpha^{(n+1)} = \mathcal{B}_\alpha \boldsymbol{\sigma} \mathbf{p} \varphi_\alpha^{(n+1)} \quad (50)$$

and finally both components are orthonormalized together via the Gram-Schmidt method considering the symmetries of the Dirac spinors. The symmetries are the same as in the Skyrme-Hartree-Fock calculations which are time reversal invariance, parity and z-signature. These symmetries furthermore prevent the solution from "slipping" into the Dirac sea. In case of a Dirac spinor these symmetries result in parity properties summarised in Table II which corresponds to the Dirac spinor ansatz in spherical symmetry written in [22].

	x=0	y=0	z=0
Re $\varphi_\alpha(\mathbf{r}, +\frac{1}{2})$	+	+	p_α
Im $\varphi_\alpha(\mathbf{r}, +\frac{1}{2})$	-	-	p_α
Re $\varphi_\alpha(\mathbf{r}, -\frac{1}{2})$	-	+	$-p_\alpha$
Im $\varphi_\alpha(\mathbf{r}, -\frac{1}{2})$	+	-	$-p_\alpha$
Re $\chi_\alpha(\mathbf{r}, +\frac{1}{2})$	-	-	$-p_\alpha$
Im $\chi_\alpha(\mathbf{r}, +\frac{1}{2})$	+	+	$-p_\alpha$
Re $\chi_\alpha(\mathbf{r}, -\frac{1}{2})$	+	-	p_α
Im $\chi_\alpha(\mathbf{r}, -\frac{1}{2})$	-	+	p_α

TABLE II: Parity properties of the Dirac spinor with respect to the coordinate planes

For a comparison the energy of homogeneous asymmetric nuclear matter is calculated similar to [23].

C. Numerical Procedure

The numerical method for solving the equations for the baryonic wave functions (49) and (50) is essentially the same as in the case of the Skyrme Hartree–Fock approach. Thus we restrict the discussion in this section to the solution of the meson field equations (35) and add some comments on the imaginary time step.

The meson equations have been solved with a finite difference scheme employing the conjugate gradient iterator operating on the meson fields with periodic boundary conditions. The conjugate gradient iterator has the numerical advantage that there is no operator matrix needed but only the operation of the differential operator on the meson field. The conjugate gradient method has been developed to solve linear equations [24, 25] and is now applied to a whole variety of numerical problems for example to finite element solver for elliptic boundary value problems on an adaptive mesh with hierarchical basis preconditioning [26], which provides a very fast algorithm. The main idea of the conjugate gradient step is to solve the linear equation $Ax - b = 0$ with the linear operator A and a vector b by searching the minimum of the quadratic form

$$q(x) = \frac{1}{2}x^T Ax - b^T x. \quad (51)$$

In order to search the solution numerically one can use an iteration scheme following the gradient method. Then it was discovered that the iteration is accelerated if one searches not straight in gradient direction but in the hyper-plane perpendicular to all previous directions. Theoretically the conjugate gradient step converges in less or equal steps than the dimension of the vector space. In practical applications the machine errors require a restart after a certain amount of steps.

The overall numerical procedure has a good convergence. In the imaginary time step the step Δt for $\lambda = \Delta t/\hbar$ could be set to 4.0×10^{-24} s which is even larger compared to the corresponding Skyrme calculations. In the test runs we obtained results with the parameter set L-HS which agree with [16] within numerical accuracy. We used this parameter set also for the actual calculations to compare the main properties of the relativistic mean field with the Skyrme calculations in the Wigner–Seitz cell.

IV. PAIRING CORRELATIONS

Various properties of a neutron star, like e.g. its fluidity, the opacity with respect to neutrino propagation etc., are very sensitive to occurrence of pairing correlations. Therefore we included the possible effects of pairing in all calculations. Our special attention was focussed on isospin $T = 1$ pairing for nucleon pairs with total momentum equal to zero in the 1S_0 partial wave like in an earlier approach in a spherical box [8]. Using the standard BCS approach the pairing gap Δ_k for pair of nucleons with momenta k and $-k$ is obtained by solving the gap equation[27]

$$\Delta_k = -\frac{2}{\pi} \int_0^\infty dk' k'^2 V(k, k') \frac{\Delta_{k'}}{2\sqrt{(\epsilon'_k - \epsilon_F)^2 + \Delta_{k'}^2}}. \quad (52)$$

Here $V(k, k')$ denotes the matrix elements of the NN interaction in the 1S_0 partial wave, ε_k the single particle energy for a nucleon with momentum k and ε_F the Fermi energy.

Instead of using the matrix elements of a realistic NN-interaction which is fit to the scattering data we have decided to use the density dependent zero range effective interaction by Bertsch and Esbensen [28]:

$$V(\mathbf{r}_1, \mathbf{r}_2) = V_0 \left(1 - \kappa \left(\frac{\rho(\mathbf{r}_1)}{\rho_0} \right)^\alpha \right) \delta(\mathbf{r}_1 - \mathbf{r}_2) \quad (53)$$

with the parameters $V_0 = 481 \text{ MeV fm}^3$, $\kappa = 0.7$, $\alpha = 0.45$ and the cut-off parameter for the gap-equation $\varepsilon_c = 60 \text{ MeV}$. These parameters were derived from a realistic NN interactions by Garrido et al. [29].

The occupation probabilities $\eta_k = v_k^2$ which are used to define the densities of the Skyrme Hartree-Fock or the relativistic mean field approach are determined from the quasi-particle energies E_k [9]

$$v_k^2 = \frac{1}{2} \left(1 - \frac{\varepsilon_k - \varepsilon_F}{E_k} \right) \quad (54)$$

$$u_k^2 = \frac{1}{2} \left(1 + \frac{\varepsilon_k - \varepsilon_F}{E_k} \right) \quad (55)$$

with

$$E_k = \sqrt{(\varepsilon_k - \varepsilon_F)^2 + \Delta_k^2}, \quad (56)$$

in which the pairing gap Δ_k , the single particle energy ε_k and the Fermi energy ε_F enters. The BCS-equations have to be solved in a self-consistent procedure fixing the Fermi energy ε_F by the particle number condition for N nucleons:

$$N = \sum_k v_k^2. \quad (57)$$

From the coefficients u_k and v_k of the standard BCS approach [9] and the corresponding single-particle wave functions φ_k one can calculate the anomalous density

$$\chi(\mathbf{r}) = \frac{1}{2} \sum_k u_k v_k |\varphi_k(\mathbf{r})|^2. \quad (58)$$

For a zero range pairing interaction as the one of eq.(53), a a local gap function can be defined:

$$\Delta(\mathbf{r}) = -V(\mathbf{r}) \chi(\mathbf{r}). \quad (59)$$

The pairing correlations for continuous asymmetric nuclear matter have been evaluated using the techniques described in [27, 30].

V. RESULTS AND DISCUSSIONS

In the first part of this section we are going to discuss the results of Hartree-Fock calculations using the Skyrme force with the parameter set SLy4 as defined in [10]. The calculations are performed in a Wigner Seitz (WS) cell with a shape of a cubic box. The size of the box

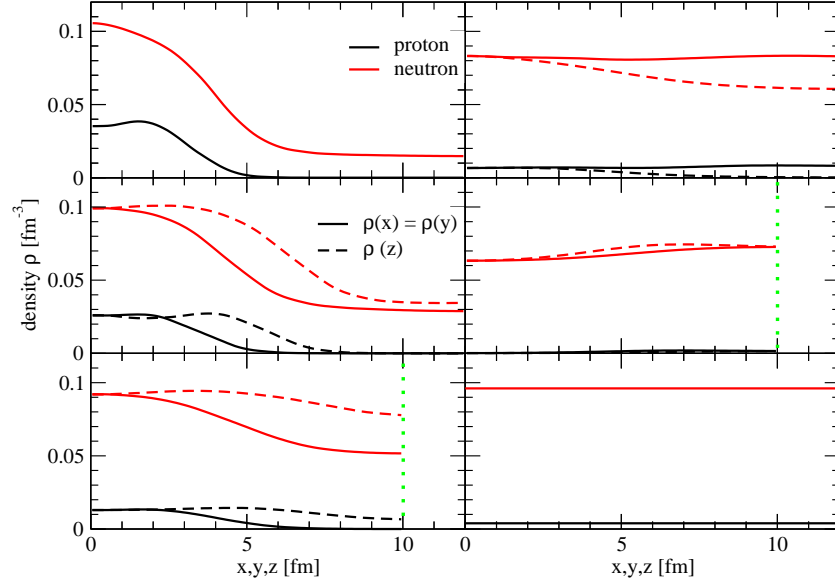


FIG. 1: (Color online) Density distributions resulting from Skyrme HF calculations for protons (black color) and neutrons (red color) as a function of cartesian coordinates x, y, z . The panels in the left column refer to densities 0.0166 fm^{-3} (top), 0.0317 fm^{-3} , and 0.0565 fm^{-3} (bottom), while those in the right column are obtained for baryon densities 0.0681 fm^{-3} (top), 0.079 fm^{-3} , and 0.1 fm^{-3} . Further discussion in the text.

R has been assumed to be identical in all 3 cartesian directions and has been adjusted to minimise the total energy per nucleon for the density under consideration. The calculations have been performed for charge neutral matter containing protons, electrons and neutrons in β -equilibrium.

A few typical density distributions resulting from these variational calculations are displayed in Fig. 1 with densities increasing from top to bottom and all densities displayed in the left column being larger than those in the right part of the figure.

We start our discussion with the top panel in the left column representing a nuclear structure at a baryonic density of 0.0166 fm^{-3} . In this case the density profiles are identical in all 3 cartesian directions. This means that we obtain a quasi-nuclear structure with spherical symmetry in the center of the WS cell. The proton density drops to zero at a radial distance of around 4 fm. The neutron density profile drops around the same radius from a central density of around 0.1 fm^{-3} to the peripheral value of around 0.01 fm^{-3} . This means that at this density we have obtained a structure of quasi-nuclear droplets forming a cubic lattice, which is embedded in a sea of neutrons.

The second panel in the left part of Fig. 1 displays the density distributions, which have been obtained at a density of 0.0317 fm^{-3} . In this case we obtain deformed quasi-nuclear droplets with radii, which are slightly larger in one direction (chosen to be the z -direction, dashed curves) than in the other two, which means that we find prolate deformation.

At slightly larger densities the deformation of the quasi-nuclear structures increase until we reach a density at which the proton density does not vanish along one of the three axis. Such an example (baryon density 0.0565 fm^{-3}) is displayed in the bottom panel of the left column. In this case we have quasi-nuclear structures in the shape of rods parallel to the z -axis. The density of these rods is not homogeneous along the symmetry axes. Note that

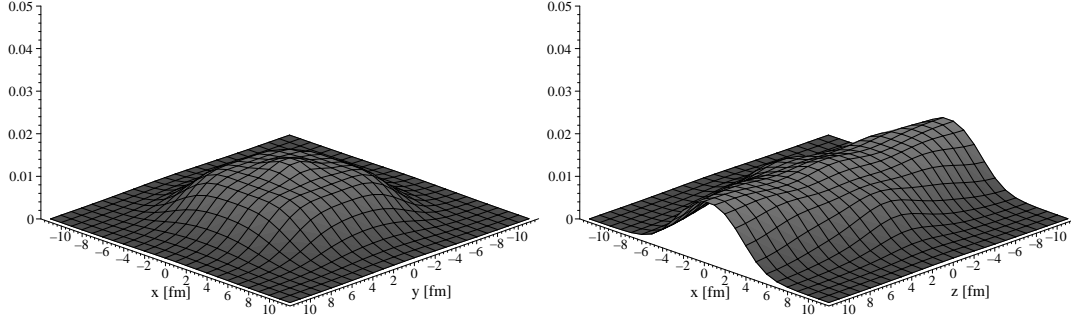


FIG. 2: Profiles for the proton density distribution forming a rod-structure at a density of 0.0625 fm^{-3} .

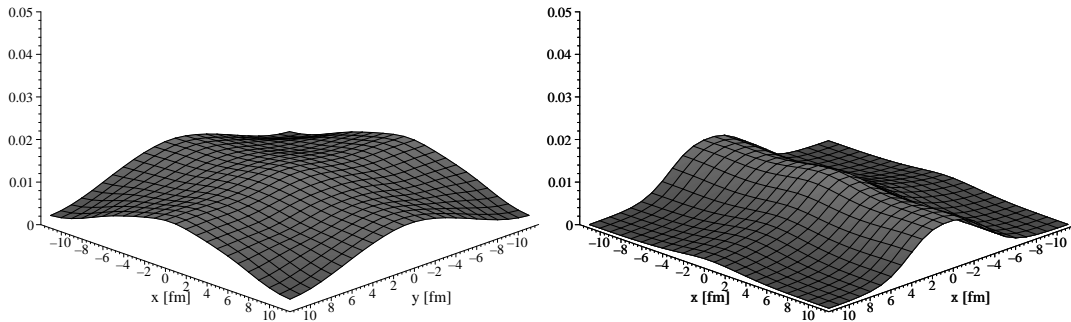


FIG. 3: Profiles for the proton density distribution forming a slab-structure at a density of 0.0775 fm^{-3} .

in this example size of the WS cell became so small ($R=10 \text{ fm}$) that the distance from the center to the boundary of the WS box lies within the range displayed in this figure and therefore has the boundary been indicated by the dotted line in this panel. This structure is also displayed in Fig. 2, where the profile of the proton-density is displayed in the xy and xz plane, respectively.

Performing HF calculations at a density of 0.0681 fm^{-3} led to a density density distribution as displayed in the top panel of the right column in Fig. 1. In this example the proton as well as the neutron density is essentially constant in the $(x, y, z = 0)$ plane. As a function of the third coordinate (z , dashed lines) the proton density is reduced from the central value at $z = 0$ to zero at the border of the WS cell and also the neutron density is reduced by about 25 percent going from the central to the peripheral values of z . Therefore in this case we observe a structure in form of parallel slabs. This slab structure is also displayed in Fig. 3. From this presentation in particular it gets obvious that the density within such a slab at $z = 0$ is not really a constant but drops in particular along the diagonals of the WS cell with $x = y, z = 0$.

At even larger densities the Skyrme Hartree-Fock calculations in a cubic WS cell yield structures, with smaller neutron densities in the center of the WS cell as compared to the boundaries. An example of such an inverse structure, which corresponds to bubbles in the sea of nuclear matter, is displayed in the second panel of the right column of Fig. 1 at a density of 0.079 fm^{-3} . The proton density, which is hardly visible in this example, drops from a peripheral value of around 0.004 fm^{-3} to a central value of zero.

As a final example we present in the bottom panel of the right column of Fig. 1 the results

	Skyrme		RMF	
	HF	TF	H	TF
droplet-rod	0.042	0.066	0.070	0.062
rod-slab	0.070	0.078	-	-
slab-homogeneous	0.080	0.085	0.075	0.072

TABLE III: Comparison of densities at which shape transitions occur using the Skyrme and Relativistic Mean Field (RMF) approach. Results are compared, employing the microscopic Hartree-Fock (HF), Hartree (H) or the Thomas-Fermi (TF) approach. All entries are presented in fm^{-3} .

of the HF calculation at a baryonic density of 0.1 fm^{-3} . At this and larger densities, the variational calculation yields homogeneous nuclear matter in β -equilibrium. This example also demonstrates that the cartesian box allows for a clean representation of the limit of homogeneous matter. This is in contrast to calculations employing a spherical WS cell. Depending on the boundary conditions used, calculations within such a spherical box can lead to density profiles, which either show a maximum or a minimum at the boundary. Even if one tries to use a set of boundary conditions, which minimise this effect, the resulting density profile does not correspond to the homogeneous solution [8].

From this discussion we see that the HF calculations in a cartesian WS cell for densities in the range of 0.01 fm^{-3} to 0.1 fm^{-3} leads to quite a variety of shapes and quasi-nuclear structures with smooth transitions in between. Following the discussions above these structures may be characterised as quasi-nuclei, rod-structures, slab structures (all embedded in a sea of neutrons) and, finally, the homogeneous matter. The densities at which the transitions from one shape to other occur according to our Skyrme HF calculations are listed in table III. The transition densities are very similar to those obtained in [31].

The energies per nucleon and the proton abundances resulting from Skyrme Hartree-Fock calculations are displayed in the lower and upper panel of Fig. 4, respectively. The solid lines indicate the results for the evaluation of homogeneous matter in β -equilibrium. The results of calculations performed in cubic WS cells are presented in terms of individual symbols. Those symbols, which scatter around the homogeneous matter results are obtained from WS calculations, constraining the HF single-particle wave functions to plane waves. Therefore the scattering of these homogeneous matter calculations within WS cells of finite size around the homogeneous result for infinite matter is a measure of the shell-effects in the WS calculations on the calculated energy and proton abundances.

The Hartree-Fock calculations, which allow for the formation of inhomogeneous quasi-nuclear structures, lead to a reduction of the calculated energy of 1 to 2 MeV per nucleon. This gain in energy is reduced with increasing density up to the density of 0.085 fm^{-3} at which the energies of the inhomogeneous structures merge into the results for the homogeneous matter. At densities below this value of 0.085 fm^{-3} the balance between the gain in binding energy due to a local increase of the baryon density and the loss of binding energy due to the localisation of nucleons and surface effects favours the occurrence of inhomogeneities in the baryon densities.

This balance between bulk energy arising from the energy density of nuclear matter treated in a local-density approximation and surface effects is also contained in the Thomas-Fermi (TF) approach. In this section we want to investigate to which extent the results

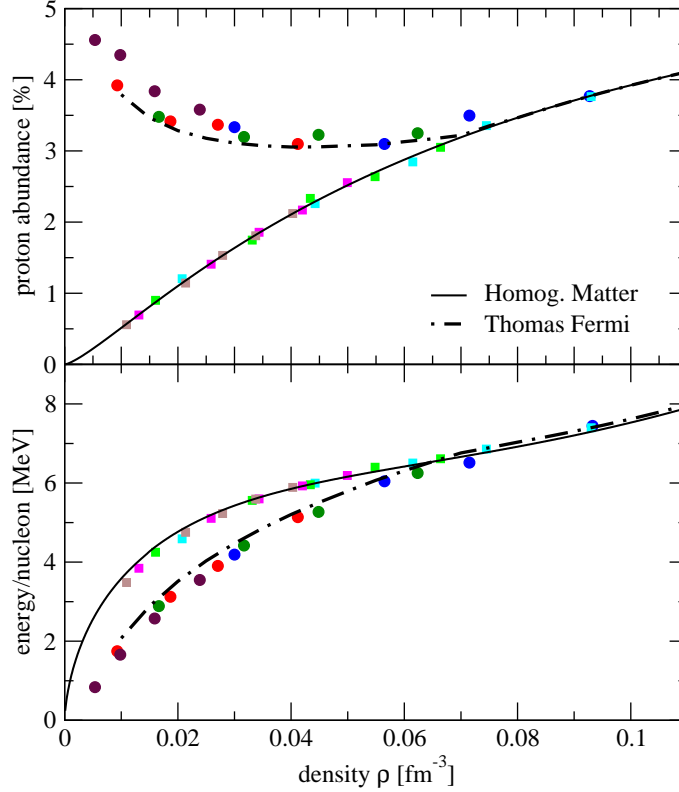


FIG. 4: (Color online) Proton-abundances and energy per nucleon as obtained from Skyrme Hartree-Fock calculations at different densities. The results evaluated in cubic Wigner Seitz cells (various symbols) are compared to those of homogeneous infinite matter (solid lines) and of Thomas-Fermi calculations. Further details are given in the text.

of our Hartree-Fock calculations can be reproduced by corresponding TF calculations. For that purpose we consider simple parametrisations for the density distribution for protons and neutrons, which contain a constant peripheral density ρ_q^{out} ($q = p$ or n for protons and neutrons, respectively) and an inner part describing the density distribution in the center of the WS cell. For spherical quasi-nuclear structures we employ the parametrisation of [4]

$$\rho_q(r) = \begin{cases} (\rho_q^{in} - \rho_q^{out}) \left[1 - \left(\frac{r}{R_q} \right)^{t_q} \right]^3 + \rho_q^{out}, & r < R_i \\ \rho_q^{out}, & R_q \leq r. \end{cases} \quad (60)$$

As an alternative we also consider a Wood-Saxon density parametrisation of the form

$$\rho_q(r) = (\rho_q^{in} - \rho_q^{out}) \left[1 + \exp \left(\frac{r - r_q}{a_q} \right) \right]^{-1} + \rho_q^{out}. \quad (61)$$

For the description of rod-shape quasi-nuclear structures we use cylindrical coordinates and parametrise the dependence of the densities on the radial coordinate in a way corresponding to eqs.(60) or (61). In the case of quasi-nuclear structures in form of slab-shapes these parametrisations are considered for the dependence of the densities on the cartesian coordinate z .

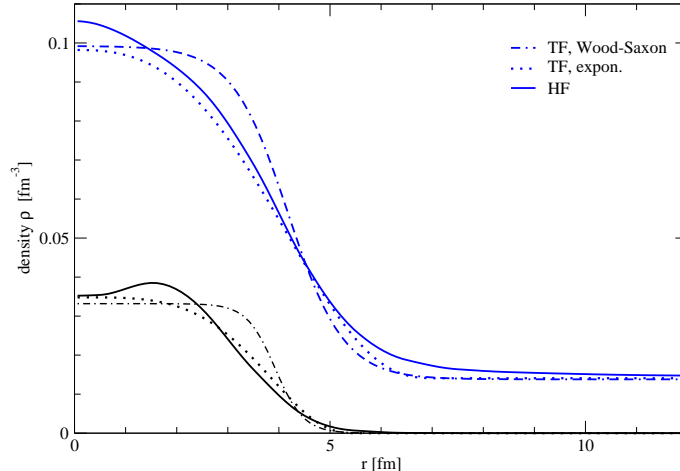


FIG. 5: (Color online) Density distributions resulting from Skyrme HF calculations for protons (black color) and neutrons (blue color) as a function of the distance from the center of the Wigner Seitz cell. The densities resulting from HF are compared to those determined in Thomas-Fermi (TF) calculations, assuming the parametrisation of (60), dotted line, and (61), dashed line. The example refers to a global baryon density of 0.0166 fm^{-3} .

Assuming those density distributions, the TF energy is calculated as a sum of the bulk-energy, i.e. the integrated nuclear-matter energy densities, plus the contribution of a surface term of the form [3, 4]

$$E_{\text{surf}} = F_0 \int_{\text{WS-cell}} d^3r |\nabla \rho|^2. \quad (62)$$

The parameters of the density distributions in (60) and (61) are varied to minimise the energy of the system under consideration. The Parameter F_0 for the surface energy term in (62) has been adjusted in two different ways. In a first approach we have considered the properties of the nucleus ^{208}Pb and adjusted F_0 in such a way that the TF calculation reproduced the energy and radius of this nucleus derived from Skyrme HF. This leads to a value of F_0 of 68.3 MeV fm^5 and 59.7 MeV fm^5 using the parametrisation of eq.(60) and the Wood-Saxon parametrisation of eq.(61), respectively.

Adjusting the surface parameter F_0 in this way, one can evaluate the energies of quasi-nuclear structures in a WS cell using the TF approximation. The results for these TF energies are presented by the dashed dotted line in the lower panel of Fig. 4. One finds that this procedure leads to energies, which are consistently larger than those obtained in the HF calculations. It seems that the TF approach, as it is used here, is underestimating the gain in energy due to the formation of inhomogeneous structures. This could be a general problem of the TF approximation or a result of the limitation in the variational ansatz for the density functions.

To investigate these possibilities we have considered the different parametrisations displayed in eqs.(60) and (61). It turns out that these two parametrisations lead indeed to different density distributions, as displayed in the example of Fig. 5, but it turns out that the resulting energy predictions do not exhibit significant differences, so that we present only one example for the TF approach in Fig. 4.

We then readjusted the the surface term in (62) to obtain an optimal fit of the HF energies

for the quasi-nuclear structures in β -equilibrium. This readjustment of the surface term leads to values of the surface parameter F_0 , which are about a factor of one half smaller than obtained from the fit to the properties of ^{208}Pb . Using these readjusted surface parameter we observe critical densities for the shape transitions of the quasi-nuclear structures from droplets to rods to slabs and to homogeneous nuclear matter at values which are similar to the results obtained in the HF calculations. If, however, one uses this reduced values derived from the fit to inhomogeneous matter in β -equilibrium the TF calculation do not give an accurate description of Hartree-Fock energies, in which the proton abundance has been fixed e.g. to a value of 10 percent. This result can be taken as an indication that in addition to the iso-scalar surface term of (62) an iso-vector surface term might be required in addition to obtain a reliable TF approximation to the results of corresponding HF calculations over a wide range of proton-neutron asymmetries.

The upper panel of Fig. 4 contains results on the proton abundances for baryonic matter plus electrons in β -equilibrium. The value of the proton abundance assuming homogeneous matter increases with density reaching a value of about 4 percent at a baryonic density of 0.1 fm^{-3} . Allowing for inhomogeneous, however, this value is almost constant around 3.2 percent in the density interval from 0.03 to 0.08 fm^{-3} and yields even larger values for densities below 0.03 fm^{-3} . This trend is also reproduced in the TF calculations. The increase of the proton abundances at smaller global densities reflects the fact that at those small densities we observe local structures in the center of the WS cells, with large local densities. The proton abundance in these quasi-nuclear droplets is significantly larger than the proton abundance in the homogeneous matter with the same global density. The scattering of the results for the proton abundances as a function of density resulting from the HF calculations reflects the shell-effects, which preferentially yield quasi-nuclear with closed shells for the protons.

A comparison of energies resulting from relativistic mean field calculations in a Wigner Seitz cell are displayed in the lower panel of Fig. 6. Comparing these results with the corresponding values displayed in Fig. 4 one finds that the energy gain due to the formation of inhomogeneous structures is much weaker in the relativistic mean field calculations as compared to the Skyrme model. This is also reflected in the corresponding Thomas-Fermi calculations. Note that also in this case we have adjusted the constant F_0 of the surface term in (62) to reproduce the bulk properties of ^{208}Pb as predicted by the relativistic mean field calculations. This leads to value for F_0 of 87.4 MeV fm^5 and 80.3 MeV fm^5 using the parametrisation of eq.(60) and the Wood-Saxon parametrisation of eq.(61), respectively. Both values are significantly larger than the values required for F_0 in the case of the Skyrme model used above.

The different interplay between volume-, surface-, symmetry- and Coulomb effects in the relativistic mean field model as compared to the Skyrme model also leads to smaller values for the proton abundance in the region of nuclear densities, in which inhomogeneous structures emerge. The values around $\rho = 0.02 \text{ fm}^{-3}$, displayed in the upper panel of Fig. 6, are about 40 percent smaller than the corresponding values obtained in the Skyrme model (see Fig. 4). The differences in the balance between volume- and surface-contributions to the energy also lead to different quasi-nuclear structures in the nuclear models under consideration. It is worth mentioning that within the relativistic mean field mode we do not find any formation of slab-like structures. Therefore the table III contains for this case only transition densities for droplet to rod structures and the formation of a homogeneous structure.

The density profiles obtained from these 2 approaches also yield different results. As an example we present in Fig. 7 the density profiles at $\rho = 0.032 \text{ fm}^{-3}$, a density at which both

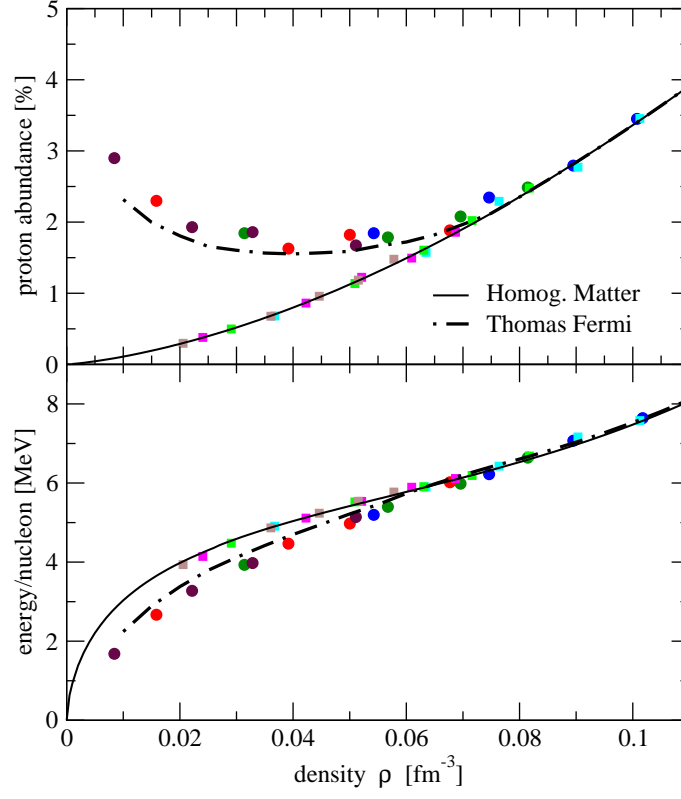


FIG. 6: (Color online) Proton-abundances and energy per nucleon as obtained from relativistic mean-field calculations at different densities. The results evaluated in cubic Wigner Seitz cells (various symbols) are compared to those of homogeneous infinite matter (solid lines) and of Thomas-Fermi calculations. Further details are given in the text.

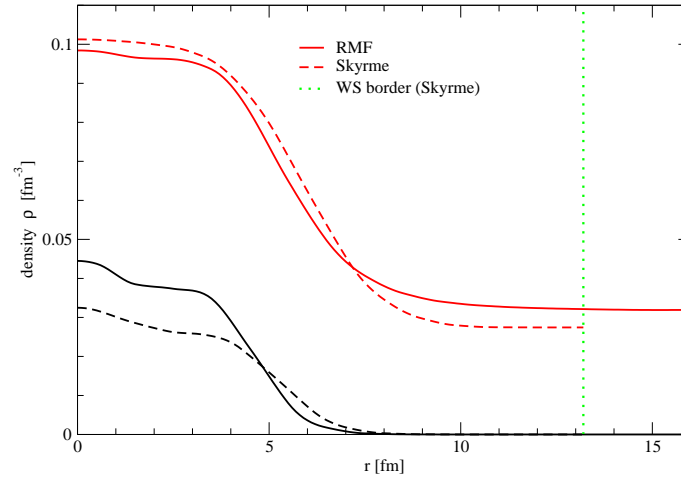


FIG. 7: (Color online) Density profiles for protons and neutrons as derived from Skyrme HF and relativistic mean field calculations at a global density of $\rho = 0.032 \text{ fm}^{-3}$.

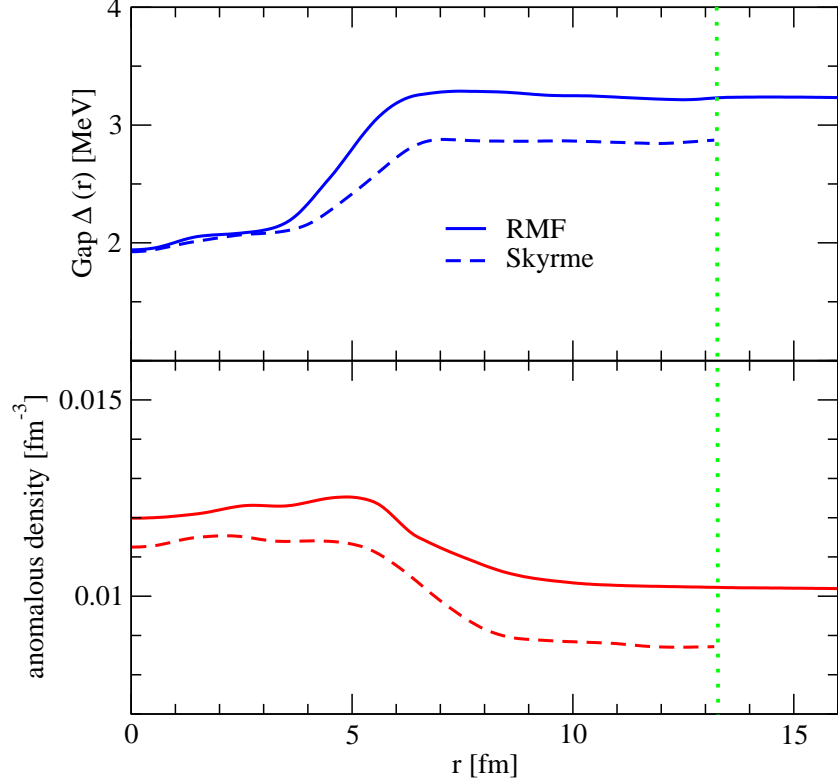


FIG. 8: (Color online) Local pairing gap $\Delta(r)$ (upper panel, see eq.(59)) and anomalous density $\chi(r)$ (lower panel, see eq.(58)) for the configurations, which are also considered in Fig. 7.

the relativistic as well as the Skyrme model yield a droplet structure. Note, that in the case of the Skyrme calculation we obtain a Wigner Seitz cell with a length of 26.4 fm which leads to a borderline as indicated by the dotted line, while the corresponding borderline for the RMF calculation is identical to the frame of the figure.

Finally, a feature of the pairing correlations obtained in these calculations shall be discussed. For that purpose we present in the upper panel of Fig. 8 the local pairing gap $\Delta(r)$ (see eq.(59) for the formation of neutron pairs, as obtained in the Skyrme and relativistic mean field model at $\rho = 0.032 \text{ fm}^{-3}$. In both of these approaches one observes a suppression of the local gap $\Delta(r)$ in the region of the quasi-nuclear structure, i.e. in the region where the density is large.

This phenomenon has been observed before[8, 31, 32, 33] and has lead to discussions about various phenomena, which are related to to this periodic structure of the gap parameter. It should be noted, however, that this suppression of the gap parameter in the high-density region of the quasi-nuclear structure is either to the local-density approximation, which is used to calculate this local gap or to the assumption of the density-dependence of the interaction strength for the pairing interaction, like the one, which we have considered in our calculations (see eq.(53)). If, rather than looking at the local gap parameter $\Delta(r)$, we inspect the anomalous density $\chi(r)$ (see eq.(58)), one finds even a small enhancement of the anomalous density in the region of the quasi-nuclear structure. This suggests that the reduction of the pairing gap in the region of high densities might be an artefact of the special

interaction considered.

VI. CONCLUSIONS

The structure of neutral baryonic matter is investigated in a region of baryon densities between 0.01 and 0.1 fm^{-3} performing various Hartree-Fock and mean-field calculations with inclusion of pairing correlations in a periodic lattice of Wigner-Seitz (WS) cells of cubic shapes. In this region of densities, which should occur in the crust of neutron stars, one observes structures ranging from neutron-rich nuclei embedded in a sea of neutrons up to homogeneous matter. The symmetries of the WS cell allow the formation of triaxial structures but also include rod- and slab-like structures and provide a natural transition to the description of homogeneous matter.

For the baryonic components a Skyrme Hartree-Fock approximation has been considered as well as a relativistic mean field model. Both approaches yield an intriguing variety of quasi-nuclear structures with smooth transitions in between. The occurrence of special structures as well as the critical densities at which transitions between those structures occur depend on the nuclear model considered.

The resulting energies as well as the proton abundances can fairly well be reproduced by a Thomas-Fermi approach, if the constant, determining the strength of the surface term is adjusted to reproduce the results of the microscopic calculations. A surface term depending on the isospin asymmetry might be required to obtain Thomas-Fermi results, which are reliable over a large interval of proton-neutron asymmetries.

Pairing-correlations have been evaluated within the BCS approach, assuming a density-dependent contact interaction. This leads to local pairing gaps for neutron pairing, which are significantly smaller in the regions of the quasi-nuclear structures as compared to the bulk of the neutron sea. It is argued, however, that this feature might be an artefact of the density-dependence of the effective pairing interaction.

The present studies provide an interesting starting point for further studies on the properties of matter in the crust of neutron stars. The single-particle energies and wave-functions could be used for a microscopic study of response-functions, which allow e.g. the evaluation of neutrino opacities.

This has been supported by the European Graduate School “Hadrons in Vacuum in Nuclei and Stars” (Basel, Graz, Tübingen), which obtains financial support by the DFG.

-
- [1] C.J. Pethick and D.G. Ravenhall, *Ann. Rec. Nucl. Part. Sci.* **45**, 429 (1995).
 - [2] M. Hashimoto, H. Seki, and M. Yamada, *Prog. Theor. Phys.*, **71**, 320 (1984).
 - [3] K. Oyamatsu, *Nucl. Phys. A* **561**, 431 (1993).
 - [4] K. Oyamatsu and K. Iida, *nucl-th/0609040*.
 - [5] T.H.R. Skyrme, *Nucl. Phys.* **9**, 615 (1959).
 - [6] D. Vautherin and D.M. Brink, *Phys. Rev.* **C5**, 626, (1972).
 - [7] P. Bonche and D. Vautherin, *Nucl Phys. A* **372**, 496 (1981).
 - [8] F. Montani, C. May, and H. Müther, *Phys. Rev.* **C69**, 065801 (2004).
 - [9] P. Ring and P. Schuck, *The Nuclear Many Body Problem*, (Springer, New York, 1980).
 - [10] E. Chabanat, P. Bonche, P. Haensel, J. Meyer, R. Schaeffer, *Nucl. Phys. A* **635**, 231, (1998).

- [11] P. Bonche, H. Flocard, P.-H. Heenen, S.J. Krieger, M.S. Weiss, Nucl. Phys. **A443**, 39 (1985).
- [12] K.T.R. Davies, H. Flocard, S. Krieger, and M.S. Weiss, Nucl. Phys. **A342**, 111 (1980).
- [13] D. Vautherin, Phys. Rev. **C7**, 296 (1973).
- [14] J.D.Jackson, *Classical Electrodynamics* (2nd ed., Wiley, New York 1975).
- [15] P.-G. Reinhard, Rep. Prog. Phys. **52**, 439 (1989).
- [16] C.J. Horowitz and B.D. Serot, Nucl. Phys. **A368**, 503 (1981).
- [17] R. Fritz, *Korrelationen und Relativistische Effekte in Atomkernen* (Ph-D thesis, Eberhard-Karls-Universität Tübingen, 1994).
- [18] J.D. Bjorken, S.D. Drell, *Relativistic Quantum Mechanics* (McGraw Hill, New York, 1964).
- [19] M. Rufa, P.-G. Reinhardt, J. Maruhn, W. Greiner, and M.R. Strayer, Phys. Rev. **C38**, 390 (1988).
- [20] B.D. Serot and J.D. Walecka, Adv. Nucl. Phys. **16** (1986)
- [21] F. Hofmann, C.M. Keil, and H. Lenske, Phys. Rev. **C64**, 034314 (2001)
- [22] M. Kleinmann, R. Fritz, H. Mütter, and A. Ramos, Nucl. Phys. **A579**, 85 (1994).
- [23] S.S. Avancini, M.E. Bracco, M. Chiapparini, and D.P. Menezes, Phys. Rev. **C67**, 024301, (2003).
- [24] M.R. Hestenes, and E. Stiefel, Nat. Bur. Standards, J. of Res. **49**, 409 (1952).
- [25] J.K. Reid, *Large Sparse Sets of Linear Equations*, 231 (Academic Press, London and New York, 1971).
- [26] H. Yserentant, Appl. Math. Comput. **19** no. 1–4, 347 (1986)
- [27] J. Kuckei, F. Montani, H. Mütter, and A. Sedrakian, Nucl. Phys. **A723**, 32 (2003).
- [28] G.F. Bertsch and H. Esbensen, Ann. Phys. **209**, 327 (1991).
- [29] E. Garrido, P. Sarriguren, E. Moya de Guerra, and P. Schuck, Phys. Rev. **C60**, 064312 (1999).
- [30] S.A.Fayans, S.V. Tolokonnikov, E.L. Trykov, and D. Zawischa, Nucl. Phys. **A676**, 49 (2000).
- [31] P. Magierski and P.-H. Heenen, Phys. Rev. **C65**, 045804 (2002).
- [32] P. Magierski, Phys. Rev. **C75**, 012803 (2007).
- [33] M. Baldo, E.E. Saperstein, and S.V. Tolokonnikov, nucl-th/0609031.